INORGANIC CHEMISTRY FRONTIERS

CHINESE CHEMICAL SOCIETY

ROYAL SOCIETY OF CHEMISTRY

RESEARCH ARTICLE

View Article Online
View Journal | View Issue

Cite this: *Inorg. Chem. Front.*, 2026, **13**, 1715

Tm^{3+}-mediated energy bridge in lead-free double perovskites: suppressing multiphonon relaxation for multifunctional photonic applications

Jiaqi Zhao,[a] Zheng Fu,[a] Kejie Li,[a] Mengmeng Dai,[a] Zhiying Wang, *[b] Guiying Liang,[c] Yanling Wei*[c] and Zuoling Fu *[a]

The growing demand for efficient and sustainable photonic materials has spurred significant interest in eco-friendly lead-free double perovskites, which exhibit exceptional photoluminescence properties for next-generation sensing and display technologies. However, the emission performance of the material is limited by multiphonon relaxation, which leads to low energy efficiency under complex operating conditions. In this study, the $^3H_5$ energy level of Tm^{3+} is strategically engineered as an energy bridge within lead-free double perovskites, effectively overcoming the constraints imposed by inefficient multiphonon relaxation in Er^{3+} ($^4I_{11/2} \rightarrow {}^4I_{13/2}$). This targeted modulation of energy transfer pathways results in a significant 50-fold enhancement in the red-to-green (R/G) emission ratio of Er^{3+}, increasing from 0.09 to 4.58, accompanied by a pronounced chromaticity shift from green (0.278, 0.709) to red (0.678, 0.320). This tunable emission behavior is further modulated by laser power density and excitation wavelength (808 or 980 nm). Moreover, Gd_2MgTiO_6 (GMTO):Er^{3+},Tm^{3+} demonstrates excellent temperature-measuring ability based on the luminescence intensity ratio ($^2H_{11/2}/{}^4F_{9/2} \rightarrow {}^4I_{15/2}$), achieving a maximum relative sensitivity of 1.03% K^{-1} at 313 K. This work not only demonstrates a generalizable strategy to suppress multiphonon relaxation *via* lanthanide energy bridges but also paves the way for multifunctional photonic devices tailored to emerging applications in smart sensing, secure communication, and next-generation optoelectronics.

Received 2nd December 2025,
Accepted 14th December 2025

DOI: 10.1039/d5qi02407b

rsc.li/frontiers-inorganic

1. Introduction

Lanthanide-doped luminescent materials have garnered considerable attention in various fields, including solid-state lighting, bio-imaging, information encryption, and solar energy conversion, due to their unique optical properties, such as narrow emission bands, long lifetimes, and excellent photostability.[1–6] The energy transfer (ET) process between lanthanide ions is a key mechanism that regulates the luminescent performance of these materials, as it enables the manipulation of emission intensity, color, and even multifunctional integration to be manipulated.[7] However, traditional ET strategies often suffer from limitations such as low efficiency, single functionality and difficulty in achieving dynamic tuning, which restricts the further development of lanthanide-doped materials in advanced applications.[8–10] Therefore, exploring novel ET strategies to overcome these bottlenecks has become a pressing research goal. Recently, double perovskites with the general formula $A_2BB'O_6$ have emerged as promising host matrices for lanthanide doping, owing to their superior structural stability, flexible chemical composition, and unique crystal field environment.[11–13] Compared to conventional single perovskites (ABO_3) or other host materials (*e.g.*, oxides, fluorides), double perovskites offer more adjustable cation sites (A, B, and B′) with diverse coordination numbers and ionic radii, providing a versatile platform to design and optimize the spatial distribution and interaction of lanthanide ions.[14,15] This structural flexibility not only facilitates the construction of efficient ET pathways but also allows for the integration of multiple functionalities by tailoring the doping configuration and host composition. Thus, double perovskites hold great potential to serve as ideal hosts for realizing innovative ET strategies.[16,17] Currently, down-conversion (DC) luminescence in rare-earth-doped double perovskites has been extensively studied,[18–20] however, up-conversion

---

[a] *Key Laboratory of Physics and Technology for Advanced Batteries, College of Physics, Jilin University, Changchun 130012, China. E-mail: zlfu@jlu.edu.cn*
[b] *Ministry of Education Key Laboratory for Cross-Scale Micro and Nano Manufacturing, Nanophotonics and Biophotonics Key Laboratory of Jilin Province, School of Physics, Changchun University of Science and Technology, Changchun, 130022, China. E-mail: zhiyingw@cust.edu.cn*
[c] *School of Data Science and Artificial Intelligence, Jilin Engineering Normal University, Changchun 130052, China. E-mail: weiyanling@jlenu.edu.cn*

(UC) luminescence properties remain underexplored. Among halide perovskites, materials such as $Cs_2NaBiCl_6$ and other Cs-based compounds exhibit excellent UC luminescent performance, but their synthesis often requires prohibitively harsh conditions (HCl vapors, $T > 150$ °C) and degrades under standard environmental stressors (RH > 30%, $T > 85$ °C).[21] These challenges, coupled with potential toxicity concerns associated with certain halide components,[22] create a critical gap in the development of robust, scalable UC materials.

In this study, the oxide-based and lead-free halide perovskite luminescent material Gd_2MgTiO_6 (GMTO) was selected as a promising host due to its low toxicity, easy preparation, and exceptional optoelectronic properties. Rare earth ions (Er^{3+}, Tm^{3+} and Yb^{3+}) were strategically doped into the GMTO, enabling tunable UC luminescence under two near-infrared light sources (980 nm or 808 nm). Notably, the Tm^{3+} ions act as an ET-bridge, thereby effectively modulating the red-to-green (R/G) emission ratio of the Er^{3+} ions. Importantly, the UC luminescence can be controlled by adjusting the laser power density, allowing for the innovative design of a series of anti-counterfeiting and information storage patterns. Meanwhile, a series of highly sensitive thermometers based on GMTO:Yb^{3+},Er^{3+},Tm^{3+} have been developed based on the luminescence intensity ratio (LIR) temperature sensing technology, which shows promise for real-time monitoring and temperature measurement in extreme working environments. These rare earth-doped GMTO materials exhibit exceptional optical properties and significant application potential, laying a solid foundation for the advancement of multifunctional luminescent materials.

2. Experimental section

2.1 Material and reagents

Gd_2O_3 (99.8%, Beijing Chemical Factory), TiO_2 (AR, Sino pharm Chemical Reagent Co., Ltd), MgO (99.8%, Beijing Chemical Factory), H_3BO_3 (99.9%, Produced in Shanghai, China), Yb_2O_3 (99.99%, Aladdin), Er_2O_3 (99.99%, Produced in Shanghai, China), Tm_2O_3 (99.99%, Produced in Shanghai, China), anhydrous ethanol (99.99%, Aladdin). All the chemicals are used without any further purification.

2.2 Synthesis of Gd_2MgTiO_6:2%Er^{3+},$x$$Tm^{3+}$($x$ = 0%, 0.5%, 2%, 3%)

A series of Er^{3+} and Tm^{3+} co-doped GMTO compounds were synthesized by a high-temperature solid-state method. During sample preparation, 2% (by mass) H_3BO_3 was added as a flux, followed by the addition of an appropriate amount of anhydrous ethanol during grinding. Since MgO was easily volatilized at high temperature, its content in the total mixture was set to be 10% in excess. The remaining raw materials were precisely weighed in accordance with the predetermined stoichiometric ratio. Subsequently, the accurately measured samples were transferred to an agate mortar and subjected to thorough grinding for 30 minutes. The heating process was carried out in two steps. Initially, the temperature was raised from ambient to 1000 °C at a controlled rate of 10 °C min^{-1} in air. Subsequently, it was further increased to 1400 °C at a slower rate of 5 °C min^{-1} in air, and the samples were maintained at this elevated temperature for 8 h continuously. After completion of the heat treatment, the samples were left to cool naturally to room temperature. They were then retrieved and placed back into the agate mortar for an additional round of intensive grinding to ensure homogeneity. The well-prepared samples were then ready for subsequent testing and analysis.

2.3 Synthesis of GMTO:7%Yb^{3+},2%Er^{3+},$y$$Tm^{3+}$($y$ = 0.5%, 2%, 3%)

The sample preparation conditions and process were the same as those of GMTO:Er^{3+},Tm^{3+}, with raw materials still weighed according to the stoichiometric ratio.

2.4 Characterization

Powder X-ray diffraction (XRD) measurements were performed using an X-ray diffractometer equipped with Cu Kα radiation (λ = 0.15405 nm). To visualize the morphological features and analyze the elemental distribution within the samples, a field-emission scanning electron microscope (FE-SEM, model: Regulus-8100, Hitachi) integrated with an energy-dispersive X-ray spectroscopy (EDS) detector was employed. The Raman spectrum was recorded by the Renishaw *in Via* Raman spectrometer (VERTEX 80v, λ_{ex} = 532 nm). The luminescence spectra were recorded by an Andor SR-500i spectrometer (Andor Technology Co, Belfast, U.K.) equipped with a SR830 DSP lock-in amplifier and a DInGaAs1700-TE detector (1100 nm–1700 nm) and a DSi300-detector (380 nm–800 nm). The copper-constantan thermocouple and a temperature control system (TAP-02, orient-KOJI) were used to conduct temperature sensing. The decay lifetime curves of the samples were measured using an Omni-λ500 (Zolix, China) spectrometer with 808 and 980 nm (MDL-III-808/980-2 W, China) laser excitation.

3. Results and discussion

3.1 Material characterization

Ultra-bright and tunable double perovskite UC phosphors GMTO:Ln^{3+} have been synthesized *via* a high-temperature solid-state method. It can be clearly observed that the reflection peaks of the samples completely match those of ICSD#117584 of GMTO (Fig. 1a and b). Considering that the dopant ions such as Er^{3+} (0.89 Å), Tm^{3+} (0.88 Å), and Yb^{3+} (0.87 Å) have a smaller radius than Gd^{3+} (0.94 Å), the ionic radius percentage formula eqn (1)

$$D_p = \frac{R_m(CN) - R_d(CN)}{R_m(CN)} \times 100\% \tag{1}$$

where R_m and R_d denote the ionic radii of the host and dopant ions, respectively, and CN denotes the coordination number of each ionic site (CN = 6 for the above ions), can be used. The

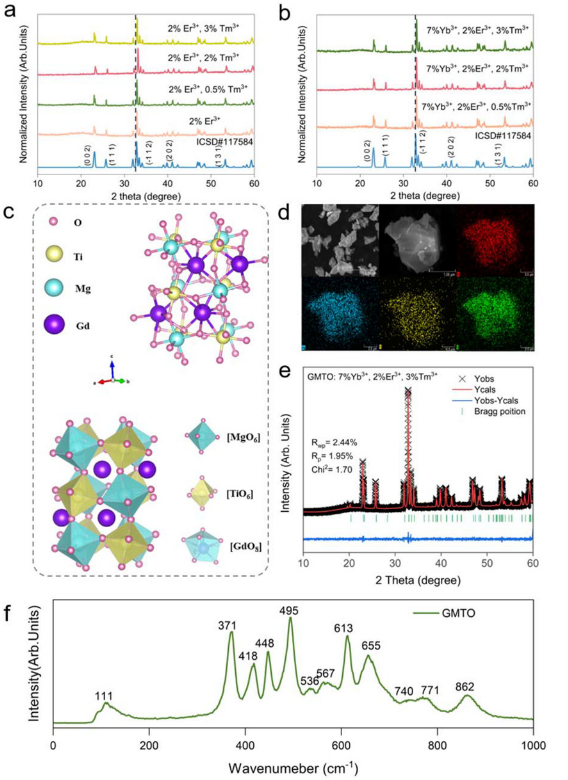

Fig. 1 Powder XRD patterns of (a) GMTO:2%Er^{3+},xTm^{3+}(x = 0–3%) and (b) GMTO:7%Yb^{3+},2%Er^{3+},xTm^{3+} (x = 0.5–3%). (c) Representative crystal structure of GMTO double perovskite. (d) FE-SEM image and elemental mapping images of the GMTO host. (e) XRD profiles for Rietveld refinement of GMTO:7%Yb^{3+},2%Er^{3+},3%Tm^{3+}. (f) Raman spectrum of GMTO host.

results showed that the D_p values of Er^{3+}/Gd^{3+},Tm^{3+}/Gd^{3+}, and Yb^{3+}/Gd^{3+} were 5.32%, 6.38%, and 7.45%, respectively. These values were significantly lower than 30%, confirming the successful substitution of the dopant ion at the Gd^{3+} site.[23,24] Furthermore, the reflection peak at 32.3° shifted to a larger angle, indicating that the lanthanide ions have been successfully doped into the host lattice (Fig. 1a).[25,26] Fig. 1c displays the crystal structure of GMTO. In this structure, [MgO_6] and [TiO_6] octahedra are alternately arranged around [GdO_8].[27] When the lanthanide ions are incorporated, the highly symmetrical host lattice is disturbed, which improves the luminescent properties of the material. It is well-known that phonons significantly influence energy level mismatches and non-radiative relaxation pathways during ET processes.[28–30] To ensure the reliability of the experimental results, FE-SEM images and the corresponding elemental mapping images of the GMTO matrix are presented in Fig. 1d. It can be seen that the constituent elements of Gd, Mg, Ti and O are uniformly distributed in the microparticles. Additionally, the XRD data of GMTO:7%Yb^{3+},2%Er^{3+},3%Tm^{3+} are analyzed using GSAS (Fig. 1e and Table S1). The refinement parameters R_{wp} and R_p are 2.44% and 1.95%, respectively, which further confirm that the synthesized sample is a pure phase. And the crystal structure (Fig. S1), FE-SEM image and elemental mapping (Fig. S2) of the GMTO:7%Yb^{3+},2%Er^{3+},3%Tm^{3+} sample also verify the successful incorporation of lanthanide dopants. The Raman spectrum of the GMTO host is presented in Fig. 1f. The phonon energy is concentrated between 350 and 740 cm^{-1} with the strongest vibration at 495 cm^{-1}, while the maximum phonon energy is located at 862 cm^{-1}.[31]

3.2 Suppression of Er^{3+} cross relaxation by introducing Tm^{3+}–$^3H_5$ level under 980 nm excitation

In Er^{3+}-only systems, the large energy gap between the $^4I_{11/2}$ and $^4I_{13/2}$ levels is predominantly depopulated *via* multiphonon relaxation, a nonradiative process that dissipates the excitation energy before efficient radiative emission can occur (Fig. 2a(i)). In contrast, the $^3H_5$ level of Tm^{3+} is well matched to the Er^{3+} $^4I_{11/2} \rightarrow {}^4I_{13/2}$ splitting and can act as an effective energy bridge, providing a competitive energy-transfer pathway that partially suppresses multiphonon relaxation. As a result, population of the Er^{3+} emitting levels is enhanced and Er^{3+}-related radiative transitions are significantly promoted (Fig. 2a (ii)). As shown in Fig. S3a, the UC emission spectra of GMTO:2%Er^{3+},xTm^{3+}(x = 0–3%) clearly exhibit the characteristic emission bands of Er^{3+} without detectable Tm^{3+} luminescence. The emissions at 530, 550 and 660 nm are attributed to the $^2H_{11/2}$, $^4S_{3/2}$ and $^4F_{9/2}$ to the ground state ($^4I_{15/2}$) transitions of Er^{3+}, respectively.[32] Without the Tm^{3+}-doping, the UC emission spectrum exhibits a dominant green emission. Fig. 2b shows that, in 2%Er^{3+},xTm^{3+}(x = 0–3%) samples under 980 nm excitation, increasing Tm^{3+} concentration leads to a progressive dominance of red emission accompanied by a pronounced rise in the R/G intensity ratio. To further verify the effective energy transfer introduced by the Tm^{3+} levels, we measured the UC decay lifetimes of GMTO:2%Er^{3+} and GMTO:2%Er^{3+},3%Tm^{3+}. As shown in Fig. 2c and d, co-doping with Tm^{3+} shortens the Er^{3+} green (550 nm) lifetime from 0.344 to 0.246 ms, whereas the red (660 nm) lifetime is prolonged from 0.852 to 1.017 ms. These opposite trends provide compelling evidence that Tm^{3+} serves as an efficient energy bridge that redistributes population from the green-emitting to the red-emitting levels of Er^{3+}. Taken together, these results demonstrate that Tm^{3+} acts as an effective mediator of Er^{3+} UC luminescence in the co-doped system, functioning exclusively as a spectral regulator rather than an emissive activator.

However, under 980 nm excitation, the emission of Tm^{3+} is inefficient. To overcome this limitation, Yb^{3+} ions are introduced as an intermediate energy bridge, which not only effectively enhances the Tm^{3+} emission but also enables an additional blue emission band of Tm^{3+} ($^1G_4 \rightarrow {}^3H_6$). This dual-sensitization strategy highlights the synergistic role of Yb^{3+} in broadening the spectral tunability of lanthanide-doped UC luminescent materials.[33,34] Similarly, as illustrated in Fig. 2f and S3c, the R/G intensity ratio of Yb^{3+}, Er^{3+},Tm^{3+} tri-doped system also exhibits an increase with the rising Tm^{3+} concentration. In order to investigate the intrinsic mechanism in GMTO:Er^{3+},Tm^{3+} and GMTO:Yb^{3+},Er^{3+},Tm^{3+} system under 980 nm excitation, the correlation between the integrated

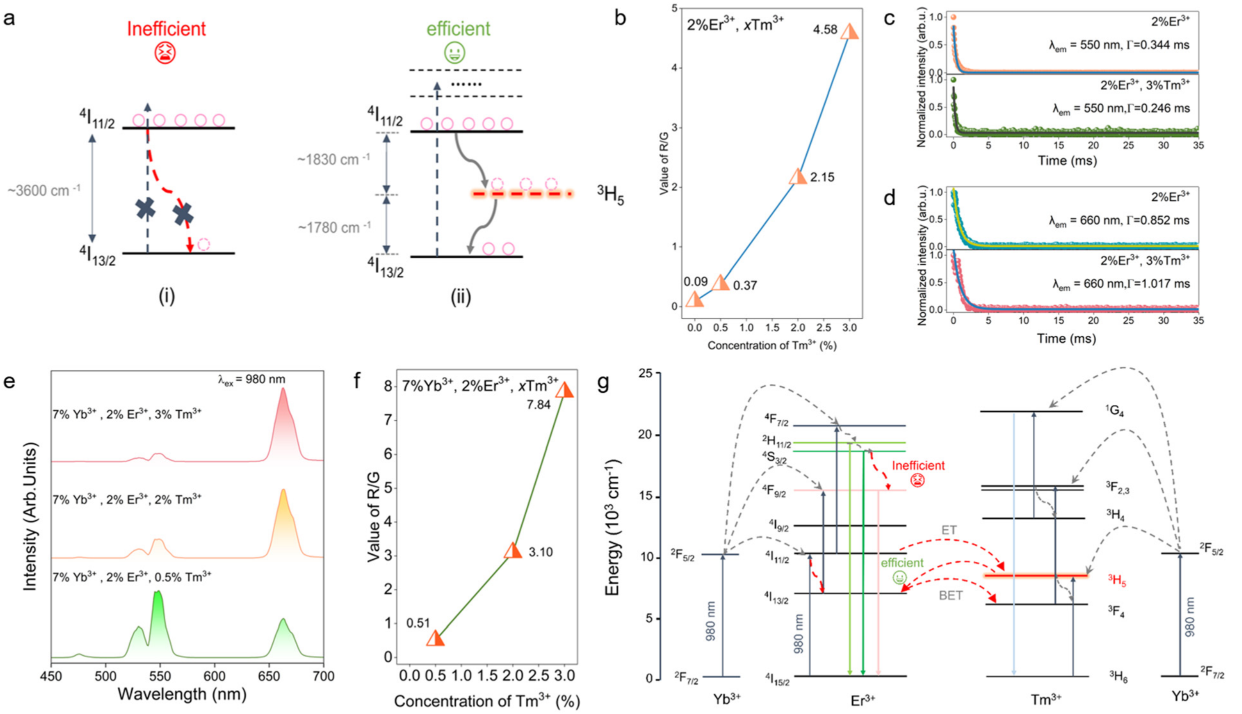

Fig. 2 (a) A schematic illustration of the regulatory role of the Tm^{3+}–$^3H_5$ energy level in UC emission of Er^{3+}. (b) R/G UC emission intensity ratio of GMTO:Er^{3+},xTm^{3+}(x = 0–3%) under 980 nm excitation. (c) UC decay lifetimes of green emission at 550 nm of Er^{3+} in the GMTO:2%Er^{3+} and GMTO:2%Er^{3+},3%Tm^{3+} under 980 nm excitation, respectively. (d) UC decay lifetimes of red emission at 660 nm of Er^{3+} in the GMTO:2%Er^{3+} and GMTO:2%Er^{3+},3%Tm^{3+} under 980 nm excitation, respectively. (e) UC emission spectra of GMTO:7%Yb^{3+},2%Er^{3+},xTm^{3+}(x = 0.5–3%) under 980 nm excitation. (f) R/G UC emission intensity ratio of GMTO:Yb^{3+},Er^{3+},xTm^{3+}(x = 0.5–3%). (g) Schematic of UC emissions of GMTO:Yb^{3+},Er^{3+},Tm^{3+} upon 980 nm excitation.

emission intensity (I) and the laser power (P) is illustrated in Fig. S3b and d. This relationship can be adequately described by the following eqn (2):[35]

$$I \propto P^n \tag{2}$$

where n represents the number of photons in the UC transitions. Based on the linear fitting results, the n values for the emissions at 478 nm, 530 nm, 550 nm, and 660 nm in the 7% Yb^{3+}, 2%Er^{3+}, 3%Tm^{3+} system are 3.00, 2.08, 1.75, and 1.67, respectively. In contrast, in the Er^{3+}–Tm^{3+} co-doped system, the fitted n values for the 530 nm, 550 nm, and 660 nm are 2.01, 1.99, and 1.30, respectively, indicating that the Tm^{3+} $^1G_4 \rightarrow {}^3H_6$ transition proceeds *via* a three-photon process, whereas the $^2H_{11/2} \rightarrow {}^4I_{15/2}$ and $^4S_{3/2} \rightarrow {}^4I_{15/2}$ transitions of Er^{3+} follow a two-photon UC mechanism. As shown in Fig. 2g, under 980 nm excitation, the Er^{3+} red emission arises from two distinct two-photon UC pathways. First, Er^{3+} ions are excited from $^4I_{15/2}$ to $^4I_{11/2}$, followed by non-radiative (NR) relaxation to $^4I_{13/2}$; subsequent excited-state absorption ($^4I_{13/2} \rightarrow {}^4F_{9/2}$) and radiative decay ($^4F_{9/2} \rightarrow {}^4I_{15/2}$) generate red emission. Secondly, Yb^{3+} ions undergo ground-state absorption ($^5F_{7/2} \rightarrow {}^5F_{5/2}$) and transfer energy resonantly to the $^4I_{11/2}$ state of Er^{3+} by resonance energy transfer (RET). Further excited-state absorption (ESA) and NR relaxation populate the higher-lying $^2H_{11/2}$, $^4S_{3/2}$ and $^4F_{9/2}$, yielding green ($^2H_{11/2}$, $^4S_{3/2} \rightarrow {}^4I_{15/2}$) and red ($^4F_{9/2} \rightarrow {}^4I_{15/2}$) emissions.

We therefore propose that introducing Tm^{3+} creates an intermediate $^3H_5$ level between the Er^{3+} $^4I_{11/2}$ and $^4I_{13/2}$ states, acting as an energy bridge. The original 3600 cm^{-1} gap is effectively split into two smaller gaps of ~1830 and ~1780 cm^{-1} by the $^3H_5(Tm^{3+})$ level. Subsequent energy transfer (ET) and back energy transfer (BET) between Er^{3+} $^4I_{11/2}$ and Tm^{3+} $^3H_5$ promote population build-up in the Er^{3+} $^4I_{13/2}$ level, enhancing the probability of excitation to $^4F_{9/2}$ (and other higher states) and thereby increasing the population density at $^4F_{9/2}$. Overall, incorporation of the Tm^{3+}–$^3H_5$ level effectively mitigates inefficient multiphonon relaxation between $^4I_{11/2}$ and $^4I_{13/2}$, establishes a bidirectional ET channel between Er^{3+} and Tm^{3+}, and significantly boosts population in the key intermediate $^4I_{13/2}$ state, leading to more efficient UC and intensified red emission. Furthermore, as shown in Fig. 2d–f, additional sensitization by Yb^{3+} enables Tm^{3+} to undergo three-photon UC to yield blue emission ($^1G_4 \rightarrow {}^3H_6$). Taken together, these results demonstrate a rational strategy for tuning UC luminescence by constructing optimized ET channels that exploit the complementary energy-level structures of Er^{3+},Tm^{3+}, and Yb^{3+}.

3.3 Photoluminescence properties upon 808 nm excitation

Owing to the rich ladder-like energy-level structure of Er^{3+}, different excitation wavelengths can selectively address distinct intermediate states, offering an additional degree of freedom for tailoring UC pathways. Building on the 980 nm pumping results, we therefore explored how exploiting this multilevel structure under 808 nm excitation could further regulate the UC behavior. Remarkable UC luminescence was observed in GMTO co-doped with Er^{3+},Tm^{3+} and Yb^{3+} under 808 nm excitation. A systematic study of the UC emission spectra and associated ET dynamics revealed significant modulation of the emission color. As shown in Fig. 3a, b and S4a, we observed a systematic increase in the R/G emission ratio. A systematic study of the UC emission spectra and associated ET dynamics revealed significant modulation of the emission. Notably, lifetime analysis (Fig. S5) confirms this finding, under 808 nm excitation, the introduction of Tm^{3+} ions regulates the energy level populations of Er^{3+}. The lifetime of Er^{3+} green emission (550 nm, $^4S_{3/2} \rightarrow {}^4I_{15/2}$) shortens from 0.546 ms (single-doped) to 0.473 ms (co-doped), attributed to efficient energy transfer from Er^{3+} $^4S_{3/2}$ to Tm^{3+}–$^3H_5$. In contrast, the red emission lifetime (660 nm, $^4F_{9/2} \rightarrow {}^4I_{15/2}$) extends from 0.937 ms to 1.738 ms, as Tm^{3+} acts as an "energy bridge" to split the large energy gap between Er^{3+} $^4I_{11/2}$ and $^4I_{13/2}$, suppressing non-radiative multiphonon relaxation and enhancing the population of the $^4F_{9/2}$ level. The power-dependent studies (Fig. S4b) provide critical insights into the UC mechanisms in GMTO:2%Er^{3+},3%Tm^{3+}. The n values for Er^{3+} emissions at 530 nm (n = 2.3), 550 nm (n = 2.01) and 660 nm (n = 1.75) confirm a two-photon excitation process. Under 808 nm irradiation, the higher photon energy enables direct population of the $^4I_{9/2}$ state in Er^{3+}. Subsequent NR relaxation processes combined with the ET and BET between Er^{3+} and Tm^{3+}, facilitate efficient energy redistribution. Notably, the Tm^{3+}–$^3H_4$ and $^3H_5$ states are found to mediate ET from Er^{3+}–$^4I_{9/2}$ to the $^4I_{13/2}$ and $^4I_{11/2}$ states. This is supported by the systematic decrease in Er^{3+} infrared emission intensity with increasing Tm^{3+} concentration (Fig. S6), indicating Tm^{3+}-mediated depletion of the $^4I_{11/2}$ population through BET processes. The observed concentration-dependent quenching behavior confirms the critical role of Tm^{3+} in modifying the Er^{3+} excited state population.

In contrast to the absorption and pumping dynamics observed under 980 nm excitation, 808 nm photon absorption shows a significantly higher probability of populating the $^2H_{11/2}$ and $^4F_{7/2}$ states compared to the $^4F_{9/2}$ level in Er^{3+} ions. As shown in Fig. 3c, under 808 nm excitation, red emission predominantly occurs *via* the relaxation of electrons from the high-energy $^4F_{7/2}$ and $^2H_{11/2}$ states rather than through a direct radiative transition from the $^4F_{9/2}$ state ($^4F_{9/2} \rightarrow {}^4I_{15/2}$). The introduction of Tm^{3+} ions plays a crucial role in modifying the energy landscape, significantly reducing the energy difference between the $^4I_{11/2}$ and $^4I_{13/2}$ states of Er^{3+}. This reduction facilitates enhanced population at the $^4I_{13/2}$ energy level through BET. In addition, Tm^{3+} ions efficiently absorb 808 nm photons, promoting transitions from the $^3H_6$ ground state to the $^3H_4$ excited state. Subsequent RET from Tm^{3+} ($^3H_4$) to Er^{3+} ($^4I_{9/2}$) and NR relaxation processes populate the $^4I_{11/2}$ state of Er^{3+}, ultimately increasing the population at the $^4I_{11/2}$ energy

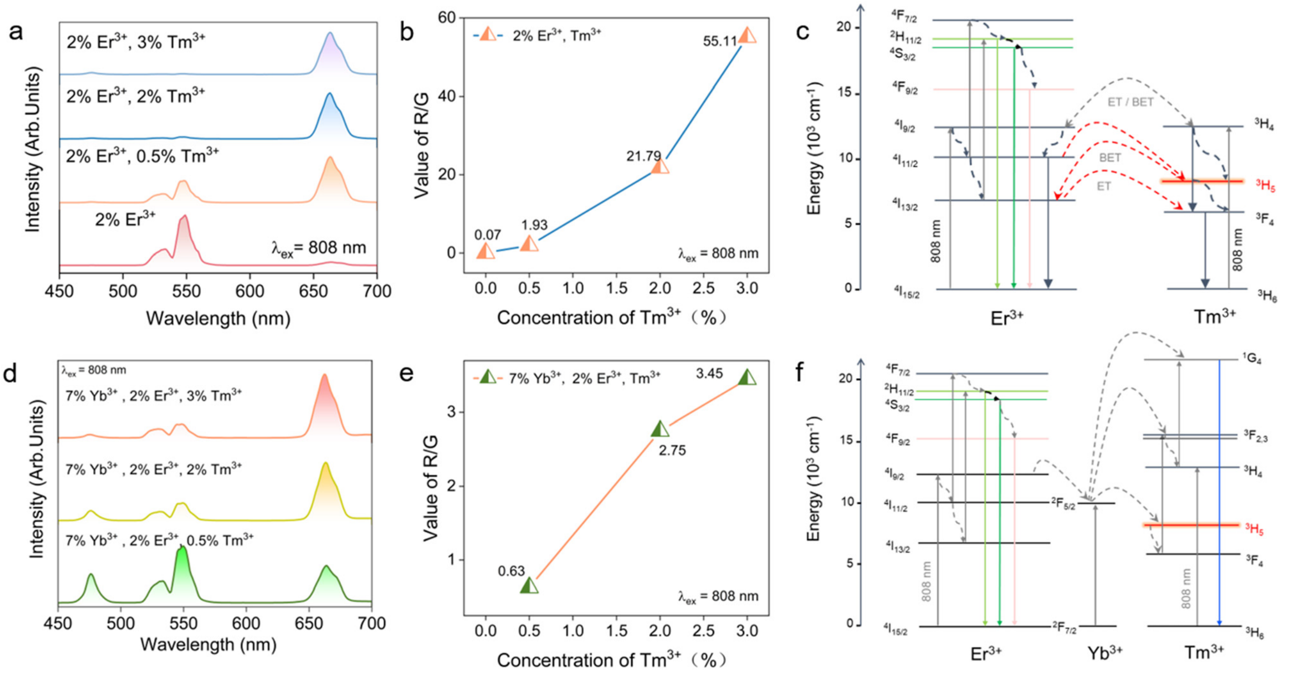

Fig. 3 (a) UC emission spectra of GMTO:2%Er^{3+},xTm^{3+}(x = 0–3%) under 808 nm excitation. (b) R/G UC emission intensity ratio of GMTO:Er^{3+},xTm^{3+}(x = 0–3%). (c) A proposed ET mechanism of GMTO:Er^{3+},xTm^{3+}(x = 0–3%) under 808 nm excitation. (d) UC emission spectra of GMTO:7% Yb^{3+},2%Er^{3+},Tm^{3+}(0.5–3%) under 808 nm excitation. (e) R/G emission ratio of GMTO:Yb^{3+},Er^{3+},xTm^{3+}(x = 0.5–3%). (f) A proposed ET mechanism of GMTO:Yb^{3+},Er^{3+},Tm^{3+} upon 808 nm excitation.

level. Thus, under 808 nm excitation, the enhanced red luminescence results from the combined effects of (i) direct Er^{3+} excitation, (ii) efficient ET from Tm^{3+} to Er^{3+} and (iii) multi-pathway energy migration processes. These mechanisms promote the population of high-energy emitting states, thereby optimizing red light generation.

Fig. 3d demonstrates that the incorporation of Yb^{3+} ions enables blue emission from Tm^{3+} under 808 nm excitation. The doping concentrations of Yb^{3+} and Tm^{3+} were found to effectively modulate Er^{3+} luminescence, and the variation in the R/G emission ratio (Fig. S4c and Fig. 3e). Notably, the presence of Yb^{3+} necessitates consideration of ET processes between Yb^{3+} and Tm^{3+}. The power-dependent studies (Fig. S4d) provide critical insights into the UC mechanisms. The n values for Er^{3+} emissions at 530 nm (n = 2.44), 550 nm (n = 2.08) and 660 nm (n = 1.87), as well as the n values for Er^{3+} emissions at 475 nm (n = 2.06), confirm a two-photon excitation process. Therefore, a proposed ET mechanism for the Yb^{3+}, Er^{3+},Tm^{3+} system under 808 nm excitation is illustrated in Fig. 3f. Our results suggest that the concentration of Tm^{3+} plays a dominant role in tuning the color of Er^{3+} UC emission. Additionally, we postulate that laser power is another critical parameter for luminescence modulation. Systematic investigations reveal that UC emission in both Er^{3+},Tm^{3+} and Yb^{3+}, Er^{3+},Tm^{3+} systems can be effectively tuned through the selection of excitation wavelength (980 nm or 808 nm) coupled with precise modulation of the laser power (Fig. S7), the R/G emission ratio in the GMTO:2%Er^{3+},0.5%Tm^{3+} phosphor displays a distinct decreasing trend as the laser power density increases from 0.5 to 4 W, which differs from the concentration-dependent tuning effects. The multimodal and tunable luminescence characteristics of GMTO:Ln^{3+} samples provide a robust theoretical and experimental foundation for future developments in information storage and fluorescence-based anti-counterfeiting technologies.[36–39] CIE coordinate analysis (Fig. S8) further quantified this wavelength-dependent and power-dependent chromaticity shift, revealing that the magnitude of color change was significantly greater under 808 nm excitation than under 980 nm excitation. These results also demonstrate the existence of an excitation wavelength/power-selective ET mechanism, highlighting the crucial role of pump wavelength optimization in tuning UC luminescence.

3.4 Temperature sensing and optical information storage

It is well established that lanthanide ions (Ln^{3+}) and transition metal ions exhibit considerable potential for applications in temperature sensing and optical anti-counterfeiting owing to their distinctive luminescence characteristics. The luminescence intensity ratio (LIR) technique relies on the thermally induced redistribution of electrons between thermally coupled levels (TCLs) or non-thermally coupled levels (non-TCLs) of these ions. Nevertheless, such systems are inherently constrained by the relatively narrow energy gaps (typically ΔE = 200–2000 cm^{-1}), which can limit their sensitivity and operational range.[40] Although non-TCL-based LIR techniques overcome the limitation of ΔE, they introduce another significant challenge: the absence of a Boltzmann distribution between the two monitored energy levels prevents the establishment of thermal equilibrium. Consequently, the ET efficiency from higher to lower energy levels adversely affects the achievable temperature sensitivity. These fundamental limitations highlight that conventional single-approach LIR thermometry inevitably faces intrinsic drawbacks, underscoring the need for innovative alternative strategies.

Building upon these facts, we conducted a comprehensive investigation of LIR thermometry by synergistic integration of both TCLs and non-TCLs, thereby achieving enhanced temperature sensing accuracy. For experimental validation, we selected GMTO:7%Yb^{3+},2%Er^{3+},0.5%Tm^{3+} phosphors, and monitored their luminescence over a broad temperature range (313–523 K) under 980 nm excitation (Fig. S9). As depicted in Fig. 4a, the temperature-dependent UC emission spectra revealed distinct thermal responses for different transitions (Fig. 4b). Specifically, the emissions from the $^1G_4 \rightarrow {}^3H_6$, $^4S_{3/2} \rightarrow {}^4I_{15/2}$, and $^4F_{9/2} \rightarrow {}^4I_{15/2}$ transitions exhibited significant thermal quenching with increasing temperature, while the $^2H_{11/2} \rightarrow {}^4I_{15/2}$ transition demonstrated remarkable thermal stability. Based on these observations, we developed a triple-mode LIR thermometric model that incorporates both non-TCLs (LIR_1 and LIR_3 to eqn (3)) and TCLs mechanisms (LIR_2 to eqn (4)). In particular, LIR_2 utilized the classic Boltzmann-distribution-based TCL approach ($^2H_{11/2}/{}^4S_{3/2}$):[32,41]

$$\mathrm{LIR} = A + B\exp\left(\frac{C}{T}\right) \tag{3}$$

$$\mathrm{LIR} = B\exp\left(\frac{C}{T}\right) \tag{4}$$

where T is the absolute temperature, A, B and C are fitting constants. The results in Fig. S10(a–c) clearly showed that the three LIRs were highly fitted to eqn (3) and (4). In these models, $LIR_{(1-3)}$ represented the intensity ratio of emissions from different transitions: $I_{(530/475\ nm)}$, $I_{(530/550\ nm)}$ and $I_{(530/660\ nm)}$, respectively. It is well known that the relative sensitivity (S_r) is commonly introduced to assess the heat-sensing capabilities of the synthesized materials. This parameter provides a precise metric for comparing thermal sensitivity characteristics among various thermometric materials. S_r is calculated as follows:[33,34,42,43]

$$S_r = \frac{1}{\mathrm{LIR}}\left|\frac{\partial \mathrm{LIR}}{\partial T}\right| \tag{5}$$

As presented in Fig. 4c, the $S_{r(max)}$ value of the three modes above reaches up to 0.95% K^{-1} in LIR_2 and LIR_3 at 313 K.

The temperature-dependent UC emission spectra of GMTO:7%Yb^{3+},2%Er^{3+},0.5%Tm^{3+} under 808 nm excitation were systematically investigated (Fig. 4d). Notably, the thermal response trends of the emissions closely resembled those observed under 980 nm excitation (Fig. 4e). Distinct thermal behaviors were identified for the transitions originating from $^1G_4 \rightarrow {}^3H_6$ (Tm^{3+}), $^4S_{3/2} \rightarrow {}^4I_{15/2}$ (Er^{3+}), and $^4F_{9/2} \rightarrow {}^4I_{15/2}$ (Er^{3+}), all of which exhibited pronounced thermal quenching. In con-

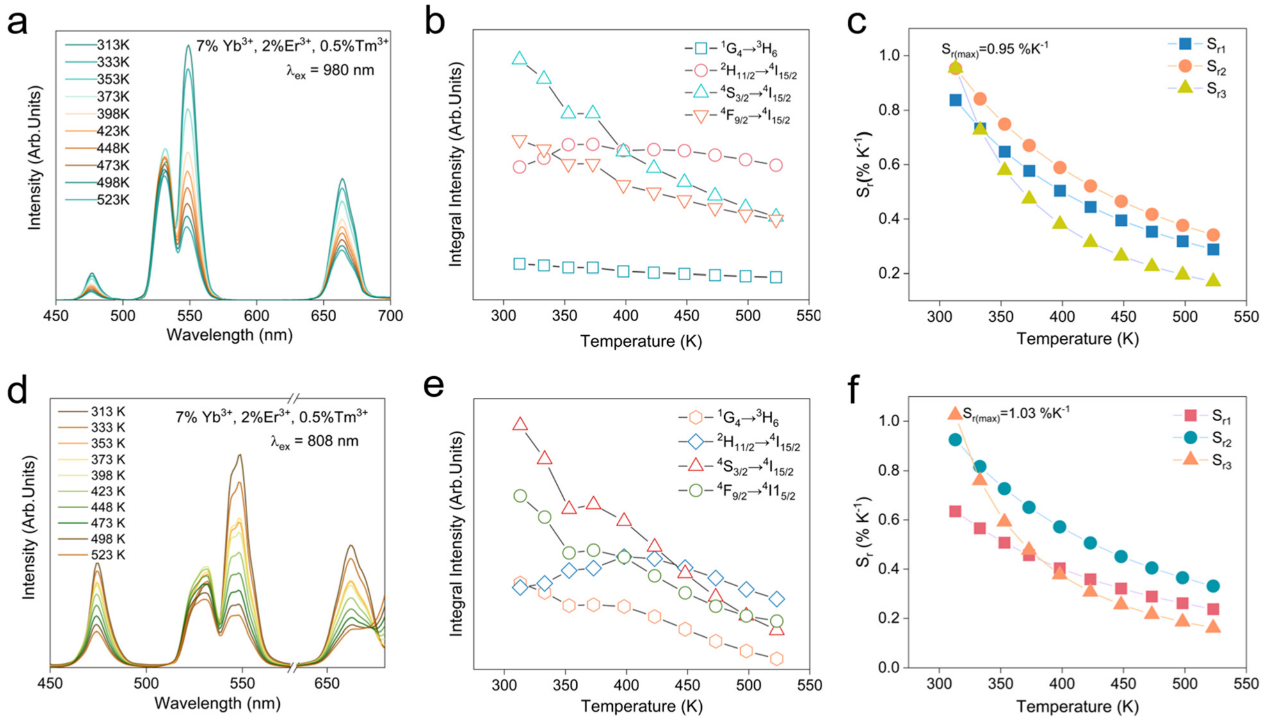

Fig. 4 (a) Temperature-dependent UC emission spectra of GMTO:7%Yb^{3+},2%Er^{3+},0.5%Tm^{3+} under 980 nm excitation. (b) The corresponding luminescence integral intensities of $^1G_4 \rightarrow {}^3H_6$, $^2H_{11/2} \rightarrow {}^4I_{15/2}$, $^4S_{3/2} \rightarrow {}^4I_{15/2}$, $^4F_{9/2} \rightarrow {}^4I_{15/2}$ under 980 nm excitation. (c) Calculated S_r values based on LIR model. (d) Temperature-dependent UC emission spectra of GMTO:7%Yb^{3+},2%Er^{3+},0.5%Tm^{3+} under 808 nm excitation. (e)The corresponding luminescence integral intensities of $^1G_4 \rightarrow {}^3H_6$, $^2H_{11/2} \rightarrow {}^4I_{15/2}$, $^4S_{3/2} \rightarrow {}^4I_{15/2}$, $^4F_{9/2} \rightarrow {}^4I_{15/2}$ under 808 nm excitation. (f) Calculated S_r values based on the LIR model.

trast, the $^2H_{11/2} \rightarrow {}^4I_{15/2}$ (Er^{3+}) transition demonstrated an initial increase in emission intensity with rising temperature, followed by quenching at elevated temperatures. These characteristics enabled the development of a robust multimodal LIR thermometry system under 808 nm excitation, similar to the three-mode LIR temperature sensing achieved under 980 nm excitation (Fig. S11(a–c)). Notably, as shown in Fig. 4f, the optimized S_r for LIR_3 reached 1.03% K^{-1} at 313 K. A comparison of the S_r obtained in this study with those reported in previously published works was provided in Table S2, further confirming the excellent temperature-sensing performance of the proposed thermometer. In addition, GMTO:Yb^{3+},Er^{3+},Tm^{3+} exhibits outstanding thermal stability, as demonstrated by its performance over heating–cooling cycles between 333 K and 423 K. And the temperature uncertainty (δT) is a critical parameter for optical temperature sensing, the formula is as follows:[44]

$$\delta T = \frac{1}{S_r}\frac{\delta \mathrm{LIR}}{\mathrm{LIR}} \tag{6}$$

The δT of GMTO:Yb^{3+},Er^{3+},Tm^{3+} reflects the precision of its temperature measurement ability. As displayed in Fig. S12, the LIR value is obtained by 50 times consecutive tests at 333 K. The δT values of LIR are 0.53 K. Our findings demonstrated that GMTO:Yb^{3+},Er^{3+},Tm^{3+} phosphors not only possessed dual-excitation capability (808/980 nm) but also enabled high-performance multimode LIR-based temperature sensing under dual-mode excitation.

Leveraging the dual-mode excitation properties and the tunability of the UC luminescence *via* modulation of doping concentration and laser power (Fig. S13), we have developed strategies for advanced optical anti-counterfeiting and information storage applications. As illustrated in Fig. 5a, our design utilizes GMTO:Yb^{3+},Tm^{3+} and GMTO:Yb^{3+},Er^{3+},Tm^{3+} phosphors with precisely tailored doping concentrations, patterned into clover and sun motifs. These phosphors exhibit distinct chromatic responses under alternating 980 nm and 808 nm laser excitation, enabling dynamic color-switching within the encoded patterns. This functionality provides a robust platform for high-security optical encryption and multiplexed data storage. Fig. 5b schematically depicts the laser power-dependent color modulation of the UC emission in GMTO:2%Er^{3+},3%Tm^{3+}, highlighting its exceptional potential for rewritable optical storage and related photonic applications. The capability to tune emission color in real time *via* excitation power allows for programmable spectral signatures, facilitating advanced optical encryption and establishing a new paradigm for dynamic information encoding. Furthermore, Fig. 5c demonstrates a sophisticated anti-counterfeiting application based on phosphor-mediated optical contrast. In this configuration, phosphors "I" (background) and "IV" (characters "J L U") are selectively deposited to create a dual-responsive

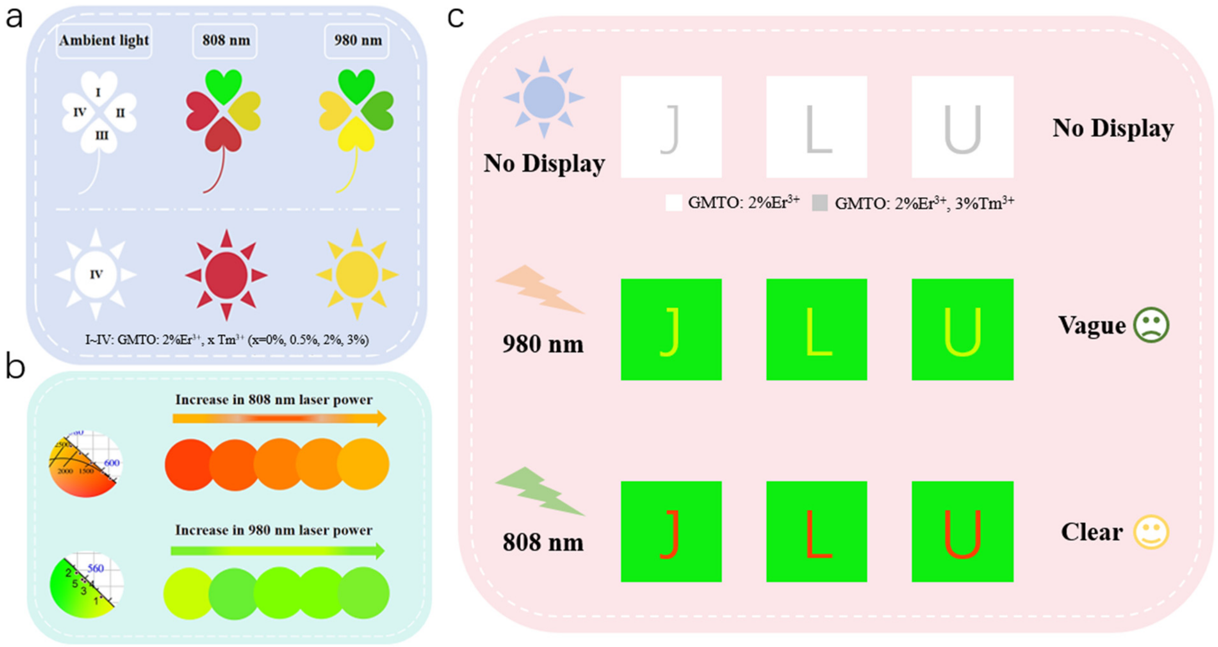

Fig. 5 Frontier applications of emission color-switchable double perovskite micro-particles. (a) Schematic of lucky clover for information encryption by using the samples with different Tm^{3+}concentrations of GMTO:Er^{3+},Tm^{3+} (0–3%). (b) Schematic of UC emission color-switching of GMTO:2%Er^{3+},3%Tm^{3+} with different laser power. (c) Coating the phosphor of "I" and "IV" on the boards. Using "I" as background, "IV" as characters of "J L U". Relying on the different changes of emission color with different excitation modes, selecting 980 nm as a pump source, vague green "J L U" will be displayed, while, selecting 808 nm as a pump source, clear yellow "J L U" will be displayed.

authentication label. Under 980 nm excitation, a faint green "J L U" pattern becomes visible, while switching to 808 nm irradiation induces a vivid red emission. This reversible high-contrast transition enables dynamic optical verification and establishes a new paradigm for secure, stimuli-responsive anti-counterfeiting technologies.

4. Conclusion

In conclusion, we have engineered a lead-free Gd_2MgTiO_6:Yb^{3+},Er^{3+},Tm^{3+} double perovskite system centered on a Tm^{3+}-mediated energy bridge, where the Tm^{3+}–$^3H_5$ state strategically mitigates the inefficient multiphonon relaxation of Er^{3+} ($^4I_{11/2} \rightarrow {}^4I_{13/2}$). This targeted ET modulation yields a remarkable 50-fold enhancement in the R/G emission ratio of Er^{3+} (from 0.09 to 4.58) compared to Er^{3+}-single-doped GMTO under 808 nm excitation, accompanied by a dramatic chromaticity shift from green (0.278, 0.709) to red (0.678, 0.320). Integrating Yb^{3+} further enables multidimensional optical control: by tuning excitation wavelength (808/980 nm) and laser power, we achieve programmable multicolor emission, which exhibits robust potential for laser-encoded anti-counterfeiting and rewritable optical storage. Moreover, the optimized GMTO:7%Yb^{3+},2%Er^{3+},0.5%Tm^{3+} phosphor demonstrates exceptional thermometric performance, with a maximum relative sensitivity of 1.03% K^{-1} at 313 K. This work establishes a generalizable strategy to suppress multiphonon relaxation *via* lanthanide energy bridges, demonstrates a single lead-free matrix integrating dynamic upconversion tuning, high-sensitivity thermal sensing, and optical encryption, and formulates design principles for phonon-engineered energy transfer in perovskite hosts. These advances that bridge spectral manipulation with multifunctional photonic applications provide a versatile platform for next-generation compact, high-efficiency optoelectronic devices in smart sensing and secure communication.

Conflicts of interest

The authors declare no competing financial interest.

Data availability

All data generated or analysed during this study are included in this published article and its supplementary information (SI). Supplementary information: detailed descriptions of LIR model, crystal structure, FE-SEM image and elemental mapping images, CIE chromatic coordinates and NIR emission spectrum. See DOI: **https://doi.org/10.1039/d5qi02407b**.

Data are available from the corresponding author on reasonable request.

Acknowledgements

This work was supported by the Natural Science Foundation of Jilin Province (YDZJ202501ZYTS607) and the National Natural Science Foundation of China (Grant No. 12374374). The authors would like to acknowledge the Instrument and Equipment Sharing Platform, College of Physics (Jilin University) for testing assistance.

References

1 R. Wu, P. Han, D. Zheng, J. Zhang, S. Yang, Y. Zhao, X. Miao and K. Han, All-Inorganic Rare-Earth-Based Double Perovskite Nanocrystals with Near-Infrared Emission, *Laser Photonics Rev.*, 2021, **15**(11), 2100218.

2 R. Zhang, Z. Wang, X. Xu, X. Mao, J. Xiong, Y. Yang and K. Han, All-Inorganic Rare-Earth Halide Double Perovskite Single Crystals with Highly Efficient Photoluminescence, *Adv. Opt. Mater.*, 2021, **9**(19), 2100689.

3 X. Li, D. Wang, Y. Zhong, F. Jiang, D. Zhao, S. Sun, P. Lu, M. Lu, Z. Wang, Z. Wu, *et al.* Halide Double Perovskite Nanocrystals Doped with Rare-Earth Ions for Multifunctional Applications, *Adv. Sci.*, 2023, **10**(20), 2207571.

4 Z. Rao, X. Zhao and X. Gong, Rare-Earth-Based Lead-Free Halide Double Perovskites for Light Emission: Recent Advances and Applications, *Adv. Funct. Mater.*, 2024, **34**(44), 2406424.

5 K. Li, M. Jia, J. Zhao, G. Zhang, D. Guo, Z. Wang and Z. Fu, Simultaneous Tailoring of Robust Anti-Thermal Quenching and High Thermometric Sensitivity in Lanthanide-Doped Cs_2NaYF_6 Double Perovskites, *Laser Photonics Rev.*, 2025, **19**, e00662.

6 Z. Zheng, J. Zhang, X. Liu, R. Wei, F. Hu and H. Guo, Luminescence and self-referenced optical temperature sensing performance in $Ca_2YZr_2Al_3O_{12}$:Bi^{3+}, Eu^{3+} phosphors, *Ceram. Int.*, 2020, **46**(5), 6154–6159.

7 F. Li, L. Tu, Y. Zhang, D. Huang, X. Liu, X. Zhang, J. Du, R. Fan, C. Yang, K. W. Krämer, *et al.*, Size-dependent lanthanide energy transfer amplifies upconversion luminescence quantum yields, *Nat. Photonics*, 2024, **18**(5), 440–449.

8 E. M. Chan, G. Han, J. D. Goldberg, D. J. Gargas, A. D. Ostrowski, P. J. Schuck, B. E. Cohen and D. J. Milliron, Combinatorial Discovery of Lanthanide-Doped Nanocrystals with Spectrally Pure Upconverted Emission, *Nano Lett.*, 2012, **12**(7), 3839–3845.

9 H.-L. Wang, Y.-L. Li, H.-H. Zou, F.-P. Liang and Z.-H. Zhu, Smart Lanthanide Metal–Organic Frameworks with Multicolor Luminescence Switching Induced by the Dynamic Adaptive Antenna Effect of Molecular Rotors, *Adv. Mater.*, 2025, **37**(29), 2502742.

10 L. Yan, J. Huang, Z. An, Q. Zhang and B. Zhou, Spatiotemporal control of photochromic upconversion through interfacial energy transfer, *Nat. Commun.*, 2024, **15**(1), 1923.

11 H. Wang, J. Yao and R. Zeng, The luminescence modulation of rare earth-doped/containing lead-free double perovskites toward multifunctional applications: a review, *Nanoscale*, 2024, **16**(14), 6837–6852.

12 N. K. Tailor, A. Listorti, S. Colella and S. Satapathi, Lead-Free Halide Double Perovskites: Fundamentals, Challenges, and Photovoltaics Applications, *Adv. Mater. Technol.*, 2023, **8**(1), 2200442.

13 V. Kumar, A. Kathiravan and M. A. Jhonsi, Beyond lead halide perovskites: Crystal structure, bandgaps, photovoltaic properties and future stance of lead-free halide double perovskites, *Nano Energy*, 2024, **125**, 109523.

14 Z.-X. Chen, Y. Chen and Y.-S. Jiang, *J. Phys. Chem. B*, 2002, **106**, 9986–9992.

15 J. Zhao, J. Gao and W. Li, A combinatory ferroelectric compound bridging simple ABO_3 and A-site-ordered quadruple perovskite, *Nat. Commun.*, 2021, **12**, 747.

16 X. Chen, J. Xu, Y. Xu, F. Luo and Y. Du, Rare earth double perovskites: a fertile soil in the field of perovskite oxides, *Inorg. Chem. Front.*, 2019, **6**(9), 2226–2238.

17 H. W. Lei, D. Hardy and F. Gao, Lead-Free Double Perovskite $Cs_2AgBiBr_6$: Fundamentals, Applications, and Perspectives, *Adv. Funct. Mater.*, 2021, **31**, 2105898.

18 Q. Liu, E. Pan, H. Deng, F. Liu and J.-F. Li, Dy^{3+} doped (K, Na)NbO_3-based multifunctional ceramics for achieving enhanced temperature-stable piezoelectricity and non-contact optical temperature sensing performance, *Inorg. Chem. Front.*, 2023, **10**(8), 2359–2369.

19 P. Du and J. S. Yu, Near-ultraviolet light induced visible emissions in Er^{3+}-activated La_2MoO_6 nanoparticles for solid-state lighting and non-contact thermometry, *Chem. Eng. J.*, 2017, **327**, 109–119.

20 W. Chen, Z. Liu, L. Shen, C. Shen, L. Ding, Z. Zhang, H. Zhang, W. Xiang and X. Liang, Design and energy transfer mechanism for single-phased Gd_2MgTiO_6: Bi^{3+}, Eu^{3+} tunable white light-emitting phosphors, *J. Mater. Sci.*, 2018, **54**, 4056–4072.

21 M. Cao, X. Zhao and X. Gong, Ionic Liquid-Assisted One-Step Large-Scale Synthesis of Cs_2ZrCl_6: CDs Composites with Tunable Multicolor Afterglow Emission, *Adv. Funct. Mater.*, 2024, **34**, 2408333.

22 I. Maietta, C. Otero-Martínez, S. Fernández, L. Sánchez, Á. González-Fernández, L. Polavarapu and R. Simón-Vázquez, The Toxicity of Lead and Lead-Free Perovskite Precursors and Nanocrystals to Human Cells and Aquatic Organisms, *Adv. Sci.*, 2025, **12**, 2415574.

23 X. Huang, B. Li and H. Guo, Synthesis, photoluminescence, cathodoluminescence, and thermal properties of novel Tb^{3+}-doped BiOCl green-emitting phosphors, *J. Alloys Compd.*, 2017, **695**, 2773–2780.

24 K. Li, H. Z. Lian, M. M. Shang and J. Lin, A novel greenish yellow-orange red $Ba_3Y_4O_9$:Bi^{3+}, Eu^{3+} phosphor with efficient energy transfer for UV-LEDs, *Dalton Trans.*, 2015, **44**, 20542–20550.

25 A. Bartkowiak, M. Runowski, A. Shyichuk, M. Majewska and T. Grzyb, Tunable yellow-green up-conversion emission and luminescence lifetimes in Yb^{3+}-Er^{3+}-Ho^{3+} multi-doped β-$NaLuF_4$ crystals, *J. Alloys Compd.*, 2019, **793**, 96–106.

26 K. Li and D. M. Zhu, Ratiometric optical temperature sensing properties based on up-conversion luminescence of novel $NaLaTi_2O_6$:Yb^{3+}, Er^{3+}/Ho^{3+} phosphors, *Mater. Res. Bull.*, 2025, **181**, 113117.

27 P. X. Gao, Z. Y. Zhou, P. Dong, Q. Li, H. H. Li, J. Wang, Z. Zhou and M. Xia, Tuning the luminescence properties of blue and far-red dual emitting Gd_2MgTiO_6: Bi^{3+}, Cr^{3+} phosphor for LED plant lamp, *J. Am. Ceram. Soc.*, 2021, **104**, 6444–6454.

28 F. K. Shang, C. H. Hu, W. Xu, L. Zhao, S. N. Zong, M. Yao, F. Z. Bai and Z. G. Zhang, Modulation of luminescence thermometry in Nd^{3+}-Yb^{3+} co-activated phosphors via engineering host matrix, *J. Alloys Compd.*, 2022, **896**, 162794.

29 C. Mi, J. J. Zhou, F. Wang and D. Y. Jin, Thermally enhanced NIR-NIR anti-Stokes emission in rare earth doped nanocrystals, *Nanoscale*, 2019, 12547–12552.

30 F. Auzel, Multiphonon-assisted anti-Stokes and Stokes fluorescence of triply ionized rare-earth ions, *J. Lumin.*, 1976, **12–13**, 715–722.

31 H. C. Yang, S. R. Zhang, H. Y. Yang, Y. Yuan and E. Z. Li, Vibrational spectroscopic and crystal chemical analyses of double perovskite Y_2MgTiO_6 microwave dielectric ceramics, *J. Am. Ceram. Soc.*, 2020, **103**, 1121–1130.

32 K. Saidi, M. Dammak, K. Soler-Carracedo and I. R. Martín, Optical thermometry based on upconversion emissions in Na_3Gd $(VO_4)_2$: Yb^{3+}-Er^{3+}/Ho^{3+} micro crystals, *J. Alloys Compd.*, 2022, **891**, 161993.

33 H. Y. Lu, J. S. Yang, D. C. Huang, Q. L. Zou, M. W. Yang, X. R. Zhang, Y. X. Wang and H. M. Zhu, Ultranarrow NIR bandwidth and temperature sensing of YOF: Yb^{3+}/Tm^{3+}phosphor in low temperature range, *J. Lumin.*, 2019, **206**, 613–617.

34 K. Li, D. Li, M. Jia, D. Guo, M. Dai, J. Zhao, G. Chen and Z. Fu, Li-Based Nanoprobes with Boosted Photoluminescence for Temperature Visualization in NIR Imaging-Guided Drug Release, *Nano Lett.*, 2025, **25**, 776–785.

35 H. X. Zhang, Y. Fan, P. Pei, C. X. Sun, L. F. Lu and F. Zhang, Tm^{3+}-Sensitized NIR-II Fluorescent Nanocrystals for In Vivo Information Storage and Decoding, *Angew. Chem., Int. Ed.*, 2019, **58**, 10153.

36 X. F. Zhao, Z. Y. Wu, Z. N. Yang, X. Yang, Y. Y. Zhang, M. H. Yuan, K. Han, C. Q. Song, Z. F. Jiang, H. Y. Wang, S. Q. Li and X. J. Xu, Dual-Wavelength Excited Intense Red Upconversion Luminescence from Er^{3+}-Sensitized Y_2O_3 Nanocrystals Fabricated by Spray Flame Synthesis, *Nanomaterials*, 2020, **10**, 1475.

37 J. I. Eldridge, Luminescence decay-based Y_2O_3: Er phosphor thermometry: Temperature sensitivity governed by multiphonon emission with an effective phonon energy transition, *J. Lumin.*, 2019, **214**, 116535.

38 N. Yamada, S. Shionoya and T. Kushida, Phonon-assisted energy transfer between trivalent rare earth ions, *J. Phys. Soc. Jpn.*, 1972, **32**, 1577–1586.

39 A. Ciric, S. Stojadinovic and M. D. Dramicanin, An extension of the Judd-Ofelt theory to the field of lanthanide thermometry, *J. Lumin.*, 2019, **216**, 116749.

40 J. H. Chung, S. Y. Lee, K. B. Shim and J. H. Ryu, White Lighting Upconversion in Tm^{3+}/Ho^{3+}/Yb^{3+} Co-Doped $CaWO_4$, *Appl. Phys. Express*, 2012, **5**, 052602.

41 Y. Tong, W. Zhang, R. Wei, L. Chen and H. Guo, $Na_2YMg_2(VO_4)_3$: Er^{3+}, Yb^{3+} phosphors: Up-conversion and optical thermometry, *Ceram. Int.*, 2021, **47**, 2600–2606.

42 A. Dogan, M. Erdem, K. Esmer and G. Eryürek, Upconversion luminescence and temperature sensing characteristics of Ho^{3+}/Yb^{3+} co-doped tellurite glasses, *J. Non-Cryst. Solids*, 2021, **571**, 121055.

43 S. Zhou, S. Jiang, X. Wei, Y. Chen, C. Duan and M. Yin, Optical thermometry based on upconversion luminescence in Yb^{3+}/Ho^{3+} co-doped $NaLuF_4$, *J. Alloys Compd.*, 2014, **588**, 654–657.

44 G. B. Nair, S. Tamboli, S. J. Dhoble and H. C. Swart, LaOF: Yb^{3+}, Er^{3+} Upconversion Nanophosphors Operating at Low Laser Powers for Nanothermometry Applications, ACS Appl, *Nano Mater.*, 2023, **6**, 15255–15265.